

An estimation-based method to segment PET images

Ziping Liu, Richard Laforest, Joyce Mhlanga, Hae Sol Moon, Tyler J. Fraum,
Malak Itani, Aaron Mintz, Farrokh Dehdashti, Barry A. Siegel,
and Abhinav K. Jha

Abstract

Tumor segmentation in oncological PET images is challenging, a major reason being the partial-volume effects that arise from low system resolution and a finite pixel size. The latter results in pixels containing more than one region, also referred to as tissue-fraction effects. Conventional classification-based segmentation approaches are inherently limited in accounting for the tissue-fraction effects. To address this limitation, we pose the segmentation task as an estimation problem. We propose a Bayesian method that estimates the posterior mean of the tumor-fraction area within each pixel and uses these estimates to define the segmented tumor boundary. The method was implemented using an autoencoder. Evaluation of the method was performed using highly realistic simulation studies conducted in the context of segmenting the primary tumor in PET images of patients with non-small cell lung cancer. In these studies, clinically realistic tumor-tracer distributions were obtained using patient-data-derived properties. A stochastic lumpy object model was used to characterize intra-tumor heterogeneity. Realism of the simulated PET images was confirmed using a two-alternative-forced-choice study with six trained readers. Quantitative evaluation using these images demonstrated that the proposed segmentation method was accurate, significantly outperformed widely used conventional methods on the tasks of tumor segmentation and estimation of tumor-fraction areas, was relatively insensitive to partial-volume effects, reliably estimated the ground-truth tumor boundaries, and demonstrated reliable performance for different clinical configurations. This proof-of-concept study demonstrates the efficacy of an estimation-based approach to PET segmentation.

Z. Liu, H. S. Moon, and A. K. Jha are with the Department of Biomedical Engineering, Washington University in St. Louis, St. Louis, MO, 63110 USA. (*Corresponding author: Abhinav K. Jha (a.jha@wustl.edu)*)

R. Laforest, J. Mhlanga, T. J. Fraum, M. Itani, A. Mintz, F. Dehdashti, B. A. Siegel, and A. K. Jha are with the Mallinckrodt Institute of Radiology, Washington University in St. Louis, St. Louis, MO, 63110.

Index Terms

Deep learning, estimation, PET segmentation, partial-volume effects, tissue-fraction effects

I. INTRODUCTION

Reliable segmentation of oncological PET images is required for tasks such as PET-based radiotherapy planning and quantification of radiomic and volumetric features from PET images [1], [2], [3]. However, tumor segmentation from PET images is challenging for several reasons such as partial-volume effects (PVEs), high system noise, and large variabilities in the shape, texture, and location of tumors [4]. The most common PET segmentation technique, manual delineation, is both labor- and time-intensive, suffers from intra- and inter-operator variability, and has limited accuracy because of the PVEs [4]. Computer-aided segmentation methods have been developed to address these issues. These include methods based on thresholding, region growing, boundary identification, and stochastic modeling [4], [5], [6], [7]. However, these methods suffer from limitations, such as requiring user inputs, sensitivity to model assumptions [8], and limited ability to model PVEs. Learning-based methods [9], [10] have been developed to address these issues. While these methods have demonstrated promise, they typically require manual segmentations for training, which are likely affected by PVEs. Thus, accounting for PVEs remains an important challenge in accurate delineation of PET images.

The PVEs in PET imaging arise from two sources: the limited spatial resolution of PET system and the finite voxel size in the reconstructed image [11]. The limited spatial resolution leads to blurred tumor boundaries. The finite voxel size results in voxels containing a mixture of tumor and normal tissue. This is also referred to as tissue-fraction effects (TFEs). A recently developed deep-learning (DL)-based technique [12], [13] has attempted to account for the PVEs arising due to system blur. However, even this method is not able to account for the TFEs. This shortcoming arises because this method, similar to most conventional segmentation methods, performs segmentation as a pixel-wise classification task. In other words, the method assigns each pixel as belonging exclusively to either the tumor or the normal tissue class and thus does not model the TFEs. Fuzzy segmentation methods have attempted to address this issue by assigning a finite number of “fuzzy levels” for pixels containing multiple tissues [14], [15]. However, these methods do not account for the fact that the tumor-fraction area (TFA) within each pixel is a continuous variable. To address this inherent limitation in existing classification-

based segmentation techniques, a method that yields a continuous estimate of the TFA within each pixel is required.

In this manuscript, we propose an estimation-based segmentation method that addresses the above-described inherent limitation of classification-based segmentation approaches. For this purpose, the segmentation problem is posed as an estimation task. The resultant method estimates the posterior mean of the TFA within each pixel. Further, through a physics-guided learning process, the method accounts for the blur arising from limited spatial resolution. The method, implemented using an autoencoder, was developed in the context of segmenting the primary tumor in [¹⁸F]fluorodeoxyglucose (FDG)-PET images of patients with non-small cell lung cancer (NSCLC).

This paper is organized as follows. In Section II, the theory of the proposed estimation-based segmentation method is presented, followed by a description of the implementation of the method using an autoencoder. In Section III, we describe the procedure to evaluate the proposed method. In Section IV, results evaluating the proposed method are presented. Section V and VI contain discussions of the results and the conclusions, respectively.

II. METHOD

A. Theory

Consider a PET system imaging a radiotracer distribution, described by a vector $f(\mathbf{r})$, where \mathbf{r} denotes the spatial coordinates. In this manuscript, we consider 2D slice-by-slice imaging, so that $\mathbf{r} = (x, y)$. The function $f(\mathbf{r})$ describes both the tumor and the rest of the regions with tracer uptake. We denote the tracer uptake in the tumor by $f_s(\mathbf{r})$. The rest of the regions are referred to as background, and uptake in the background is denoted as $f_b(\mathbf{r})$. Thus the tracer uptake can be represented mathematically as follows:

$$f(\mathbf{r}) = f_b(\mathbf{r}) + f_s(\mathbf{r}). \quad (1)$$

We define a support function for the tumor region as $s(\mathbf{r})$, i.e.,

$$s(\mathbf{r}) = \begin{cases} 1, & \text{if } f_s(\mathbf{r}) > 0. \\ 0, & \text{otherwise.} \end{cases} \quad (2)$$

The radiotracer emits photons that are detected by the PET imaging system, yielding sinogram data. Reconstruction with the sinogram yields the reconstructed image over a pixelized grid.

Denote this reconstructed image by an M -dimensional vector $\hat{\mathbf{f}}$. Thus, the mapping from the tracer distribution to the reconstructed image is given by the operator $\Theta : \mathbb{L}_2(\mathbb{R}^2) \rightarrow \mathbb{E}^M$.

Denote the PET system by a linear continuous-to-discrete operator \mathcal{H} , and let the vector \mathbf{n} describe the photon noise. Denote the reconstruction operator, quite possibly non-linear, by \mathcal{R} . The eventual reconstructed image is given in operator notation as below:

$$\hat{\mathbf{f}} = \mathcal{R}\{\mathcal{H}\mathbf{f} + \mathbf{n}\}. \quad (3)$$

In the reconstructed image, denote the pixel width by L , and the x and y coordinates of the center of the m^{th} pixel by x_m and y_m , respectively. Then the pixel basis is given by

$$\phi_m(\mathbf{r}) = \frac{1}{L^2} \text{rect}\left(\frac{x - x_m}{L}\right) \text{rect}\left(\frac{y - y_m}{L}\right). \quad (4)$$

The fractional area that the tumor occupies in the m^{th} pixel, denoted by a_m , is given by

$$a_m = \frac{1}{L^2} \int s(r) \phi_m(r) d^2r. \quad (5)$$

Our objective is to design a method that estimates this quantity a_m from the reconstructed image $\hat{\mathbf{f}}$ for all M pixels. Denote the estimate of a_m by \hat{a}_m . Further, denote the M -dimensional vector $\{a_1, a_2, \dots, a_M\}$ by \mathbf{a} , and denote the estimate of \mathbf{a} by $\hat{\mathbf{a}}$.

Estimating \mathbf{a} from the reconstructed image is an ill-posed problem due to the null spaces of the \mathcal{H} and \mathcal{R} operator. Thus, we take a Bayesian approach to estimate $\hat{\mathbf{a}}$. We first need to define a cost function that penalizes deviation of \mathbf{a} from $\hat{\mathbf{a}}$. A common cost function is the ensemble mean squared error (EMSE), which is the mean squared error averaged over noise realizations and the true values \mathbf{a} . However, in our case, the variable \hat{a}_m is constrained to lie between $[0, 1]$, and the EMSE loss does not directly incorporate this constraint. In contrast, using the binary cross-entropy (BCE) loss as the penalizer allows us to incorporate this constraint on \hat{a}_m directly, as also suggested in Creswell et al. [16]. The BCE loss between a_m and \hat{a}_m , denoted by $l_{BCE}(a_m, \hat{a}_m)$, is given by

$$l_{BCE}(a_m, \hat{a}_m) = a_m \log(\hat{a}_m) + (1 - a_m) \log(1 - \hat{a}_m). \quad (6)$$

We define our cost function $C(\mathbf{a}, \hat{\mathbf{a}})$ as the aggregate BCE loss over all pixels averaged over the joint distribution of \mathbf{a} and the noise realization $\hat{\mathbf{f}}$. Denote $\langle \dots \rangle_X$ as the expected value of

the quantity in the brackets when averaged over the random variable X . Thus, the cost function is defined as

$$\begin{aligned}
C(\mathbf{a}, \hat{\mathbf{a}}) &= \left\langle \sum_{m=1}^M l_{BCE}(a_m, \hat{a}_m) \right\rangle_{\hat{\mathbf{f}}, \mathbf{a}} \\
&= \left\langle \left\langle \sum_{m=1}^M l_{BCE}(a_m, \hat{a}_m) \right\rangle_{\mathbf{a}|\hat{\mathbf{f}}} \right\rangle_{\hat{\mathbf{f}}} \\
&= \int d^M \hat{\mathbf{f}} \text{ pr}(\hat{\mathbf{f}}) \int d^M \mathbf{a} \text{ pr}(\mathbf{a}|\hat{\mathbf{f}}) \sum_{m=1}^M \left[a_m \log(\hat{a}_m) \right. \\
&\quad \left. + (1 - a_m) \log(1 - \hat{a}_m) \right].
\end{aligned} \tag{7}$$

To estimate the point at which this cost function is minimized, we follow an approach similar to that in previous literature [17], [18]. We differentiate the cost function with respect to the vector $\hat{\mathbf{a}}$ and set that equal to zero. Because $\text{pr}(\hat{\mathbf{f}})$ is always nonnegative, the cost function is minimized by setting the derivative equal to zero, i.e.,

$$\frac{\partial}{\partial \hat{\mathbf{a}}} \left\langle \sum_{m=1}^M \left[a_m \log(\hat{a}_m) + (1 - a_m) \log(1 - \hat{a}_m) \right] \right\rangle_{\mathbf{a}|\hat{\mathbf{f}}} = 0. \tag{8}$$

This is then equivalent to performing component-wise differentiation and setting each differentiated component to 0 [17]. For the m^{th} component, this yields

$$\begin{aligned}
&\frac{\partial}{\partial \hat{a}_m} \left\langle a_m [\log(\hat{a}_m) - \log(1 - \hat{a}_m)] \right\rangle_{a_m|\hat{\mathbf{f}}} \\
&+ \frac{\partial}{\partial \hat{a}_m} \left\langle \log(1 - \hat{a}_m) \right\rangle_{a_m|\hat{\mathbf{f}}} = 0.
\end{aligned} \tag{9}$$

Define the solution to the above equation by \hat{a}_m^* . Eq. (9) yields

$$\hat{a}_m^* = \langle a_m \rangle_{a_m|\hat{\mathbf{f}}}, \tag{10}$$

or equivalently, in vector notation,

$$\hat{\mathbf{a}}^* = \langle \mathbf{a} \rangle_{\mathbf{a}|\hat{\mathbf{f}}}. \tag{11}$$

Therefore, minimizing the cost function in Eq. (7) results in the optimal estimator equivalent to the posterior mean. Note that the same estimator is obtained when the cost function is the EMSE. We can further show that this estimator is unbiased in a Bayesian sense:

$$\begin{aligned}
\bar{\hat{\mathbf{a}}}^* &= \int d^M \hat{\mathbf{f}} \text{ pr}(\hat{\mathbf{f}}) \int d^M \mathbf{a} \text{ pr}(\mathbf{a}|\hat{\mathbf{f}}) \mathbf{a} \\
&= \int d^M \mathbf{a} \text{ pr}(\mathbf{a}) \mathbf{a} = \bar{\mathbf{a}}.
\end{aligned} \tag{12}$$

Thus, we show that minimizing the cost function defined in Eq. (7) yields a posterior mean estimate of the TFA in each pixel of the reconstructed image. This estimator will be unbiased in a Bayesian sense. From the estimated TFA values, we can define a segmented map of the tumor, as described later in III-C.

B. Implementation of the estimator

Estimating the posterior mean \hat{a}^* requires sampling from the posterior distribution $\text{pr}(a|\hat{f})$. Sampling from this distribution is challenging as this distribution is high-dimensional and does not have a known analytical form. To address this issue, we constructed an autoencoder that minimized the cost function given by Eq. (7). In this autoencoder, each intermediate layer was normalized using batch normalization to stabilize the learning process. Skip connections with element-wise addition, as implemented in a recently developed U-net-based segmentation method [12], were applied to feed the features extracted in the down-sampling path into the up-sampling path to improve the learning performance. The autoencoder was trained via the Adam optimization algorithm [19]. In the various experiments mentioned below, this autoencoder was optimized with a training set using five-fold cross validation.

III. EVALUATION

Evaluating the proposed method required access to the ground-truth TFA map. For this purpose, we conducted realistic simulation studies that provided a mechanism to describe the tumor-tracer distribution potentially as a continuous object, i.e., equivalent to $f_s(r)$ in Eq. (1). From this continuous description, the TFA in each pixel can be computed using Eq. (5), thus providing the ground truth to evaluate this method. However, for rigorous and clinically relevant evaluation of the proposed method, the simulation studies need to be highly realistic. We ensured this by using clinical data to guide our simulation, and validating the realism of our simulations using an observer study, as described below. This evaluation study was an IRB-approved, HIPAA-compliant retrospective study with a waiver of informed consent.

A. Framework to simulate realistic PET images

The framework is summarized in Fig. 1. In the first step, a realistic high-resolution tumor model was developed to capture the observed variabilities in tumor properties from an actual patient population (Fig. 1a). For this purpose, we extended a simulation framework initially

proposed in Leung et al. [12]. Summarizing briefly, tumor descriptors, including shape, size, and tumor-to-background intensity ratio, were first extracted from PET images of patients with lung cancer. Tumor shape was quantified by five harmonic elliptical Fourier descriptors [20], and tumor size was quantified by diameter. The distribution of each tumor descriptor was defined using kernel density estimation. The kernel distribution of each descriptor was then sampled, and from the sampled parameters, simulated tumors were generated. In Leung et al. [12], necrosis within the tumor was modeled by assigning a lower intensity to the tumor core than the rim. We extended that framework to model intra-tumor heterogeneity more generally. We used the observation that the tracer-uptake patterns within tumors can be modeled as a combination of lumps, where the lump locations, amplitudes, and sizes are random variables. More generally, it is suitable to characterize the tracer uptake within a tumor as a random process [21]. Thus, the intra-tumor heterogeneity was modeled using a stochastic lumpy object model. This lumpy model was inspired by the original lumpy background model [22], but with some adaptations to account for intra-tumor heterogeneity. The lumpy object model is described as

$$\begin{aligned} f(\mathbf{r}) &= s(\mathbf{r}) \sum_{n=1}^N \Lambda(\mathbf{r} - \mathbf{c}_n | a_n, \sigma_n) \\ &= s(\mathbf{r}) \sum_{n=1}^N \frac{a_n}{2\pi\sigma_n^2} \exp\left(-\frac{|\mathbf{r} - \mathbf{c}_n|^2}{\sigma_n^2}\right), \end{aligned} \quad (13)$$

where $s(\mathbf{r})$ denotes the support for the tumor, N denotes the total number of lumps, $\Lambda(\cdot)$ denotes the lump function, \mathbf{r} denotes the spatial coordinate in two dimensions, and \mathbf{c}_n , a_n , and σ_n denote the center, magnitude, and width of the n^{th} lump function, respectively. To model the tracer uptake as a random process, \mathbf{c}_n was uniformly distributed within the defined tumor support, and a_n and σ_n were uniformly distributed within a pre-defined range but appropriately scaled based on the clinically extracted values of the tumor-to-background intensity ratios. All these parameters were used to generate the tumor models.

Note that the ground truth was not needed for the background. To ensure background realism, existing patient images containing the lung cavities but with no tumor present were selected as templates for the background.

In the second step (Fig.1b), realistic forward projections for the tumor and background were generated by simulating a PET imaging system. The high-resolution tumor image and the low-resolution patient image were passed through corresponding PET system models to obtain sinograms with clinically relevant count levels. The simulation modeled the major image-degrading

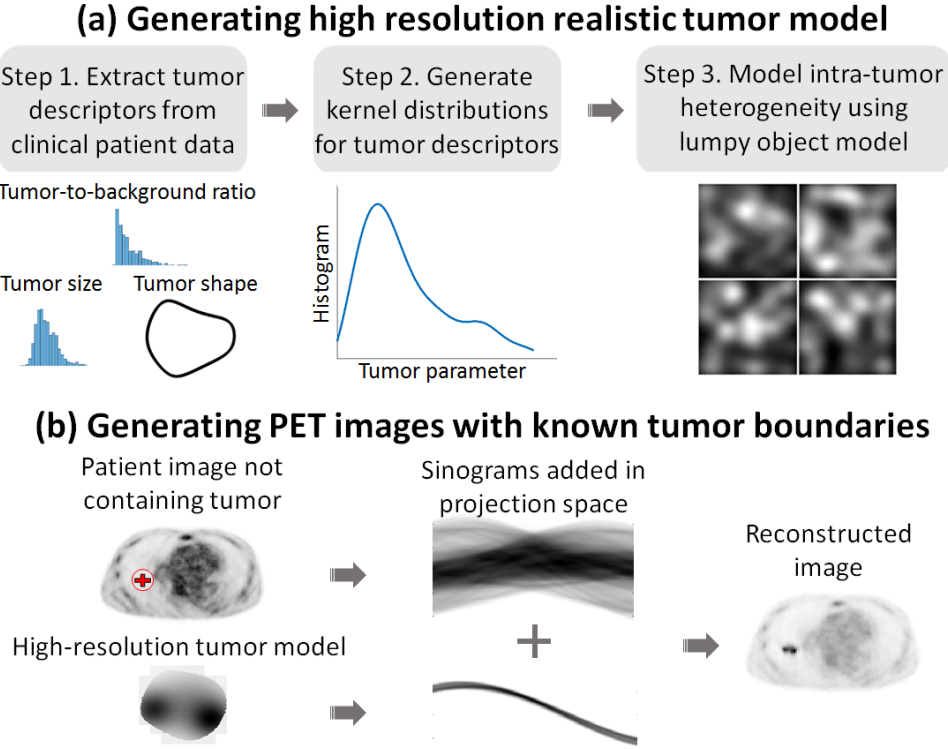


Fig. 1: Strategy for generating simulated PET images with highly realistic tumors using clinical data and a stochastic lumpy object model.

processes of system blur and photon noise. The sinograms were reconstructed using a 2D ordered subset expectation maximization (OSEM) algorithm. Similar to Ma et al. [23], adding the data in the projection space and then performing the reconstruction helped incorporate the impact of noise texture on the tumor appearance in the reconstructed image.

The next step was to validate the realism of the tumors in these simulated PET images, as we describe next.

B. Evaluating the realism of the tumors in the simulated PET images

For this purpose, we followed an approach similar to previous studies on evaluating realism of simulated tumors in CT images [23], [24]. As in those studies, our objective was to quantitatively evaluate whether trained readers could distinguish between real and simulated tumors. For this purpose, we conducted a human observer study, more specifically a two-alternative-forced-choice (2-AFC) study.

We developed a web-based app (Fig. 2) where trained readers were shown two images, one a real patient image and the other a simulated image generated using our framework. The readers were instructed that the task was to identify the image they thought had the real tumor. The tumor location was shown in the images to ensure that the readers were focusing on the tumor-realism task, and not implicitly treating this as a tumor-detection task. Additionally, the app incorporated functionalities provided by clinical software, such as providing options to invert the tumor intensities and adjust the tumor contrast, to facilitate a robust observer study. The readers were also asked to provide confidence levels for their decisions. The confidence levels are described in Table I.

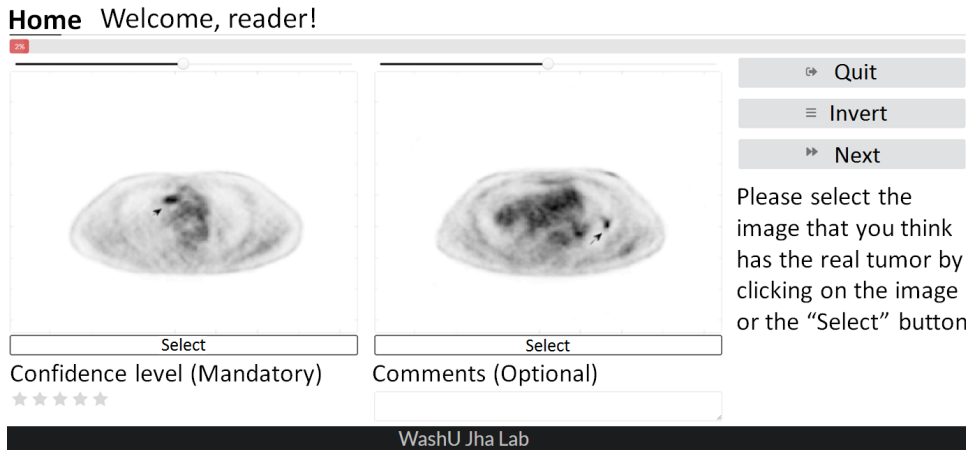


Fig. 2: Interface of the web-based application presented to readers for the 2-AFC test.

Six trained readers, which included five board-certified radiologists with specialization in nuclear medicine and many years of experience in reading clinical PET images, (B.A.S., F.D., J.C.M., T.J.F., M.I.) and one experienced nuclear-medicine physicist (R.L.), participated as readers in this study. The readers performed this test for 50 image pairs. We computed the fraction of times that each reader correctly identified the image containing the real tumor. A percent accuracy close to 50% would indicate that the simulated tumor images were as real as the patient tumor images.

The results of this study, shown in Sec. IV-A, provide evidence that the simulated images were indeed highly realistic. Thus, we used this simulation framework for evaluating the proposed segmentation method, as described next.

TABLE I: Description of the confidence levels for the 2-AFC study [23].

Confidence level	Definition
1	No confidence in decision
2	Possibly correct decision
3	Probably correct decision
4	Likely correct decision
5	100% confidence in decision

C. Evaluation of the proposed segmentation method

The proposed estimation-based segmentation method was evaluated using several studies. These studies quantitatively evaluated the accuracy of the proposed method, studied the sensitivity of the method to PVEs, compared the method to existing techniques, and also studied the performance of the method with different clinical scanner configurations. In each study, PET images with tumor were generated using the simulation framework described in Sec. III-A. The generated dataset was split into training and test sets. The autoencoder was trained and validated (five-fold cross validation) using the training dataset. The performance of the method was then evaluated using the completely independent test data set. The number of training and test images are mentioned for each study in the sections below. We first describe the metrics used to quantitatively evaluate the method.

1) *Evaluation metrics*: Since the proposed method is an estimation-based segmentation approach, the evaluation used performance metrics for both the estimation and segmentation tasks.

Performance on the estimation task was evaluated using the EMSE metric. This metric provides a combined measure of bias and variance over the distribution of true values and noise realizations, and is thus considered a comprehensive figure of merit for estimation tasks [17]. The error in the estimate of the TFA values and the tumor area was quantified using the pixel-wise EMSE and the area EMSE, respectively. The pixel-wise EMSE is given by

$$\text{Pixel-wise EMSE} = \left\langle \left\langle \|\hat{\mathbf{a}} - \mathbf{a}\|_2^2 \right\rangle_{\hat{\mathbf{f}}|\mathbf{a}} \right\rangle_{\mathbf{a}}. \quad (14)$$

The normalized area EMSE denotes the EMSE between the true and estimated areas of each tumor, normalized by the true areas. The true and estimated areas, denoted by A and \hat{A} , are

given by the \mathbb{L}_1 norms of \mathbf{a} and $\hat{\mathbf{a}}$, respectively. The normalized area EMSE is then given by

$$\text{Normalized area EMSE} = \left\langle \langle |\hat{A} - A|^2 \rangle_{\hat{\mathbf{f}}|A} \right\rangle_A. \quad (15)$$

Eq. (12) shows that the proposed method yields an estimate of the TFA that is unbiased in a Bayesian sense. To verify this, the ensemble-average bias was computed. This term, denoted by $\bar{\mathbf{b}}$, is an M -dimensional vector $\{\bar{b}_1, \bar{b}_2, \dots, \bar{b}_M\}$, with the m^{th} element of the vector quantifying the average bias of the estimated TFA in the m^{th} pixel. Consider a total of P tumor images and N noise realizations for each tumor image. Let a_{mnp} and \hat{a}_{mnp} denote the true and estimated TFAs within the m^{th} pixel for the n^{th} noise realization in the p^{th} tumor image. The m^{th} ensemble-average bias term \bar{b}_m is then given by

$$\bar{b}_m = \frac{1}{P} \sum_{p=1}^P \frac{1}{N} \sum_{n=1}^N [\hat{a}_{mnp} - a_{mnp}]. \quad (16)$$

The proximity of the elements of $\bar{\mathbf{b}}$ to 0 would indicate that the estimator was unbiased in a Bayesian sense.

Performance on the segmentation task was evaluated using spatial-overlap-, volume-, and spatial-distance-based metrics [4]. The fuzzy Dice Similarity Coefficient (fDSC) and fuzzy Jaccard Similarity Coefficient (fJSC) [25] were used to measure the spatial-overlap agreement between the ground-truth and the estimated segmentation. Higher values of the fDSC and fJSC indicate higher segmentation accuracy. The Area Similarity (AS) metric, adapted from [25] but for 2-D images, was used to quantify the similarity between the true tumor area and the tumor area measured using the proposed method. Higher values of AS indicate higher accuracy in metabolic tumor area measurement. Finally, the Hausdorff Distance (HD) was used to assess the similarity in the true boundary and the boundary generated by the segmentation technique [25]. To compute the HD, we considered only those cases where the tumor had been correctly localized by the segmentation method. Lower values of HD indicate higher accuracy in tumor-boundary delineation. Detailed definitions of these segmentation metrics are provided in Supplemental Material.

We also qualitatively assessed the performance of the proposed method on the boundary-delineation task. The estimated boundary, as defined above, was compared to the known ground truth from the continuous tumor model. The boundary was also compared to the boundary obtained with a recently developed U-net-based PET segmentation technique [12]. This U-net-

based method, similar to most conventional segmentation methods, exclusively classifies each pixel as either tumor or background.

All segmentation metrics were reported as mean values (95% confidence intervals).

2) *Comparison to other segmentation methods:* The proposed method was quantitatively compared to various commonly used semi-automated PET segmentation methods, including 40% SUV-max thresholding [5], active-contour-based snakes [6], and Markov random fields-Gaussian mixture model (MRF-GMM) [7], [26]. The method was also compared to a fuzzy segmentation technique, namely the fuzzy local information C-Means clustering algorithm (FLICM) [27]. Additionally, the method was compared to the U-net-based method described above [12]. For all the semi-automated segmentation methods, a region of interest (ROI) containing the tumor was provided as manual input. The proposed and the U-net-based segmentation method did not require any manual input and were fully automated.

To generate the simulated images for this experiment, we used 250 2-D slices from 15 patients for the background portion of the image in the simulation framework. The simulated PET imaging system was modeled with a 5 mm full-width-half-maximum (FWHM) system blur. The sinograms were reconstructed using the OSEM algorithm with 21 subsets and 2 iterations, which were selected to be similar to the PET reconstruction protocol for the patient images. The reconstructed pixel size was $4.07 \text{ mm} \times 4.07 \text{ mm}$. The autoencoder was trained and cross-validated using 6,400 images with 5-fold cross validation. Evaluation was then performed on 1,800 completely independent test images.

3) *Evaluation of sensitivity to PVEs:* To evaluate the sensitivity of the method to PVEs, we studied the performance of the method as a function of tumor size. For this purpose, all test images were grouped based on the range of the true tumor sizes. For each test image, PVE-affected tumor boundaries were generated by applying a rectangular filter to the ground-truth tumor mask. This filter modeled the resolution degradation due to the system blur and the reconstruction process. The filter size was equal to the FWHM of the Gaussian blur in a reconstructed image of a line phantom imaged using the PET system.

The total tumor area measured using the proposed method and the PVE-affected tumor area in all the test images were obtained. Each of these were divided by the true tumor area. A ratio of unity indicated that the output was insensitive to PVEs. A ratio lower or higher than unity indicated an underestimation or overestimation of the true tumor area, respectively, showing that the segmentation output was affected by the PVEs [28]. The ratios were only computed in the

cases where the tumor was localized accurately.

4) *Evaluation with different clinical configurations:* To study the performance of the proposed method with other clinical settings, we simulated two PET imaging systems with configurations similar to the Siemens Biograph 40 and Biograph Vision scanners. The PET images reconstructed from these two scanners had different pixel sizes, as dictated by the protocol. The Biograph 40 generated images of 128×128 pixels, while the Biograph Vision generated images of 192×192 pixels. Details of the PET scanner acquisition and reconstruction parameters are summarized in Table II. Clinical PET images of patients with lung cancer were obtained from these scanners. In the clinical images, slices with no tumors were identified and using these images and following the procedure described in Sec. III-A, a total of 6,240 PET images with simulated tumors were generated for each scanner. These were used for optimizing and training the autoencoder. Next, the trained network was tested on 1,560 new simulated images. The performance of the proposed approach was also compared to the U-net-based approach [12].

TABLE II: Technical acquisition and reconstruction parameters of the PET scanners (FOV: field of view).

Parameters	Biograph 40	Biograph Vision
Transaxial FOV (mm)	550	700
Axial FOV (mm)	216	162
Reconstruction method	OSEM	OSEM
Subsets	21	21
Iterations	2	2
Crystal pitch (mm)	4.00	3.30
FWHM (mm) @ 1 cm	5.90	3.70
Voxel size (mm ³)	4.30	3.65

IV. RESULTS

A. Evaluating the realism of the tumors in the simulated PET images

Fig. 3 shows representative simulated images generated using the proposed simulation framework (Sec. III-A). These images demonstrate that the framework can generate a wide variety of clinically observed tumor types, such as small tumors (top tow), tumors with multiple hot spots (middle row), and tumors with necrotic cores (bottom row).

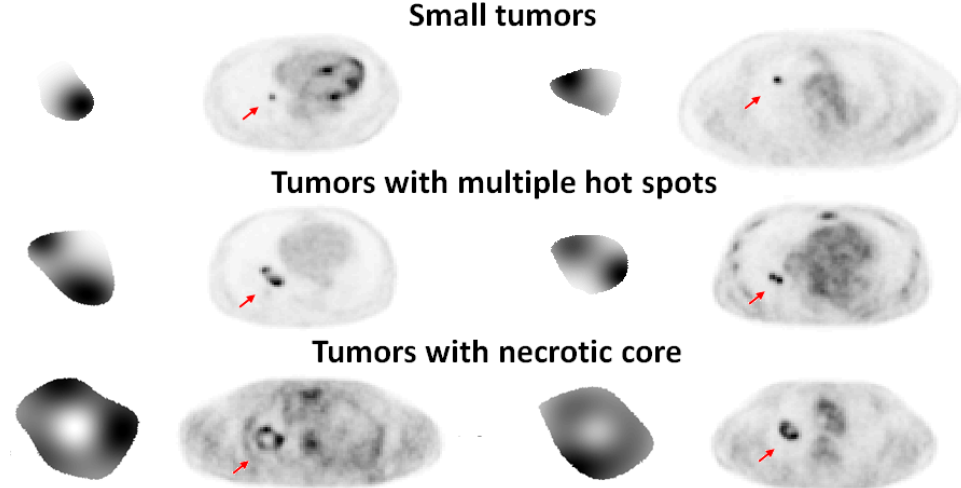


Fig. 3: Representative high-resolution tumor models with different tumor features and eventual simulated images. Tumor locations in the simulated images are marked by the red arrows.

TABLE III: Percent accuracy and mean confidence level for each trained reader participating in the 2-AFC study (NM: Nuclear Medicine).

	Percent accuracy	Mean confidence level
NM physician 1	44%	1.76
NM physician 2	50%	1.58
NM physician 3	58%	3.14
NM physician 4	58%	3.80
NM physician 5	44%	3.54
NM physicist	58%	3.52

Table III lists the results of the 2-AFC study, following the process in Sec. III-B. Each trained reader identified the real tumor accurately in only approximately 50% of the cases, indicating that it was challenging to distinguish the real and simulated tumor images. Fig. 4 shows the distributions of the confidence levels of the readers. The upper and lower rows show the distributions when correctly and incorrectly identifying the image pairs, respectively. The five board-certified radiologists with specialization in nuclear medicine correctly identified 127/250 image pairs (51% accuracy). Among the 127 correct identifications, only 42 (33%) were selected with confidence levels ≥ 4 , which indicates that the readers were not very confident even when they made correct identifications.

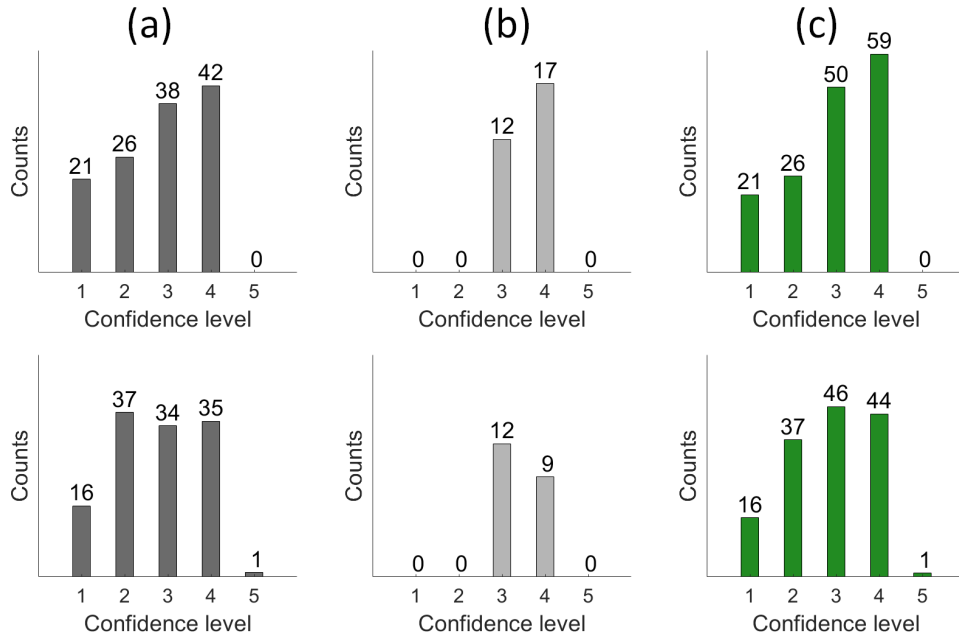


Fig. 4: Distributions of confidence levels for correctly (upper row) and incorrectly (lower row) identified pair counts for (a) five board-certified radiologists with specialization in nuclear medicine, (b) one nuclear-medicine physicist, and (c) all readers.

Examples of simulated images that were incorrectly identified by at least half of the readers but with confidence levels ≥ 3 are shown in Fig. 5. In these examples, the readers were incorrect even when confident about their decisions. This trend was observed over a range of tumor types, further demonstrating the robustness of the simulation framework in yielding realistic images. Overall, these results demonstrate that the simulated images were highly realistic.

B. Evaluating the performance of the proposed segmentation method and comparing it to other segmentation methods

Quantitatively, the proposed method significantly outperformed ($p < 0.01$) the other considered methods, including the U-net-based PET segmentation method, on the bases of the pixel-wise EMSE, normalized area EMSE, fDSC, fJSC, AS, and HD metrics (Fig. 6). The proposed method yielded the lowest pixel-wise EMSE, the lowest normalized area EMSE of 0.12, the highest fDSC of 0.79 (95% CI: 0.79, 0.80), the highest fJSC of 0.66 (95% CI: 0.66, 0.67), the highest AS of 0.90 (95% CI: 0.90, 0.90), and the lowest HD of 1.94 (95% CI: 1.90, 1.98) (Table I in Supplemental Material). In addition, all the elements of the ensemble-average bias map were

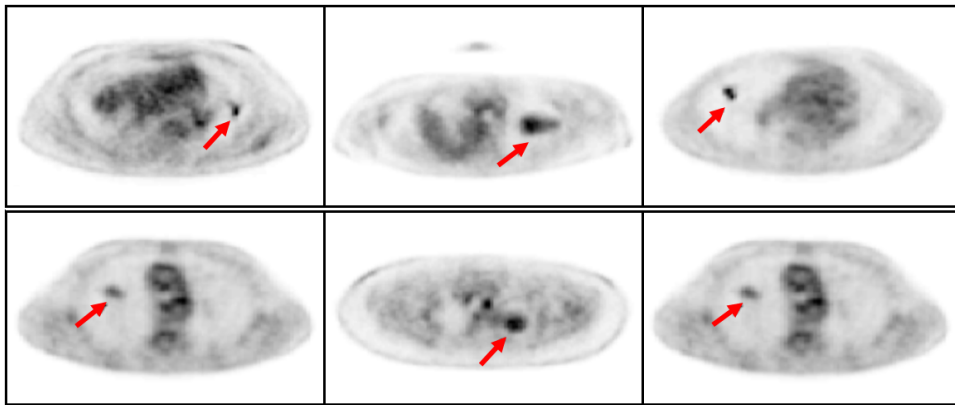


Fig. 5: Representative simulated images incorrectly identified by at least 3 readers with confidence levels ≥ 3 . Tumor locations are marked by the red arrows.

close to 0, demonstrating that the method yielded an unbiased Bayesian estimate of the TFA within each pixel.

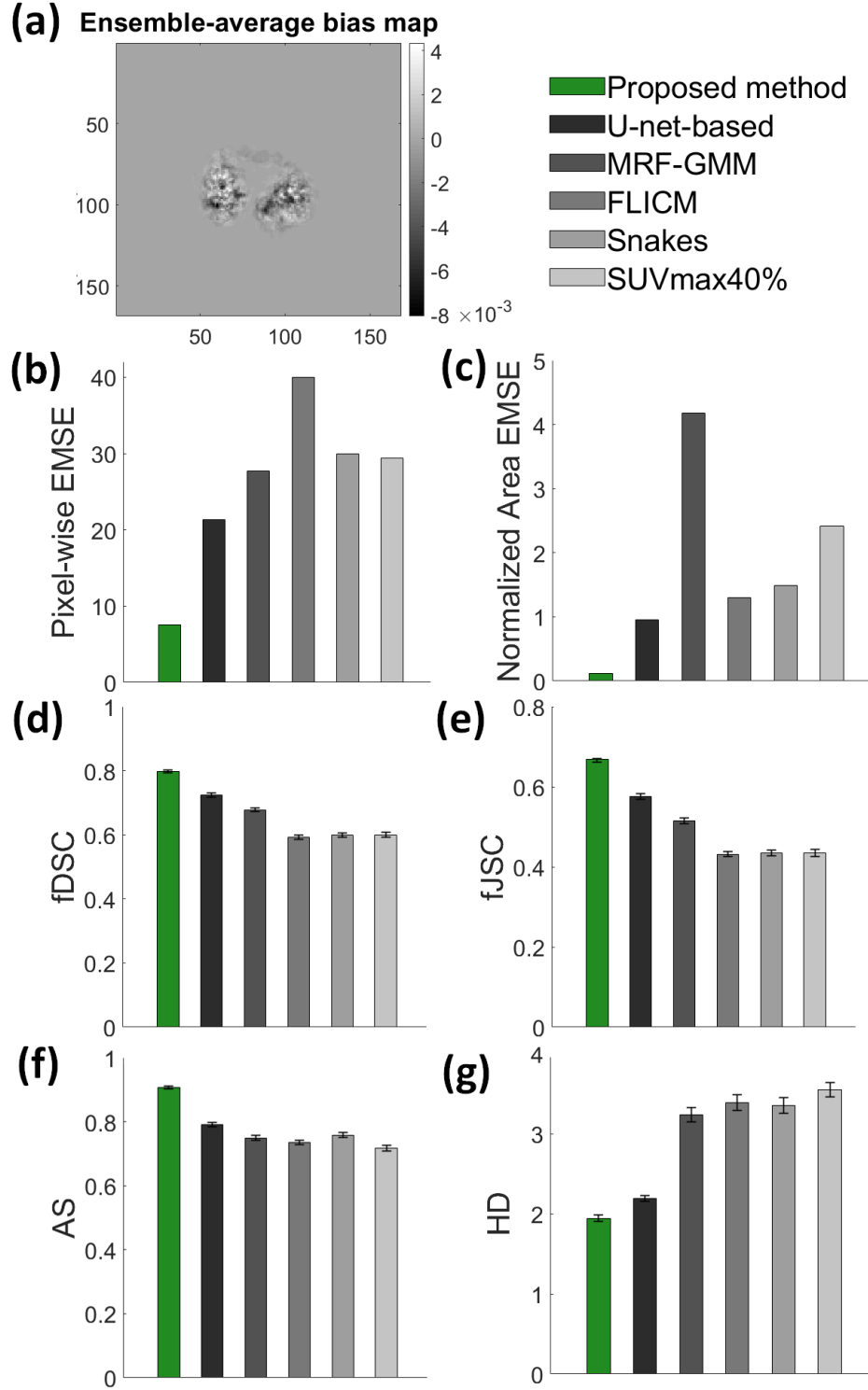


Fig. 6: (a) The ensemble-average bias using the proposed method. (b) The pixel-wise EMSE between the true and estimated tumor-fraction areas. (c) The normalized area EMSE between the measured and true tumor areas. The (d) fuzzy Dice Similarity Coefficient, (e) fuzzy Jaccard Similarity Coefficient, (f) Area Similarity, and (g) Hausdorff Distance between the true and estimated segmentations.

Fig. 7 shows the comparison between the ground-truth tumor boundaries and the boundaries yielded by the proposed method. We observe that the proposed method provides an accurate match to the ground-truth contours for different tumor types, including tumors with complex heterogeneity. Note that the boundaries yielded by the proposed method are continuous unlike the pixelated boundaries obtained with the U-net-based method. This is because our method yields a continuous estimate of the TFA for each pixel, while the U-net-based method classifies each pixel as either tumor or background.

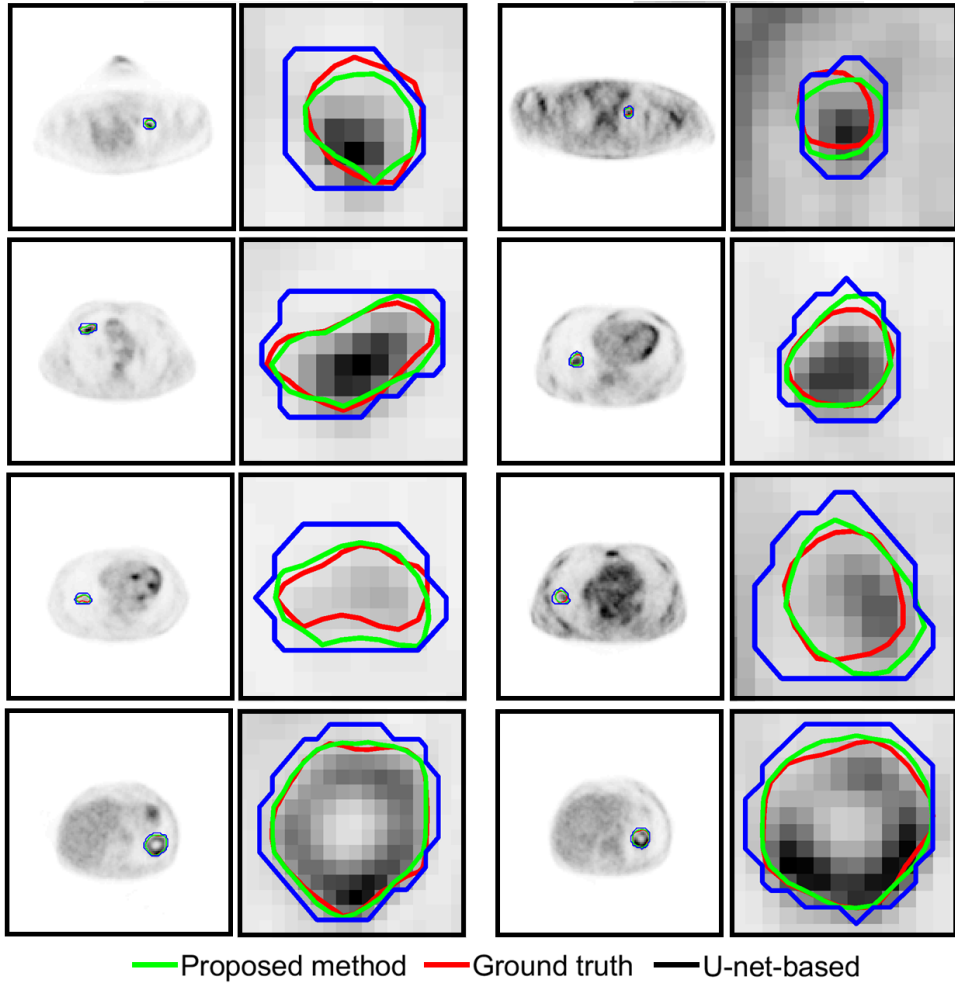


Fig. 7: Tumor contours delineated using the proposed method (green) compared to the ground-truth contour (red). Also plotted are the tumor contours obtained by the U-net-based method (blue). Zoomed contours are displayed for better visualization.

C. Evaluating the sensitivity of the proposed method to PVEs

Fig. 8 shows that the tumor area obtained with the proposed method was close to the true tumor area consistently over all tumor sizes. This was unlike the PVE-affected tumor areas, which, as expected, were significantly overestimated for smaller tumors.

Further, Fig. 9 shows that the proposed method consistently yielded the lowest normalized pixel-wise EMSE and the lowest normalized area EMSE values, where both the normalizations were performed over the true tumor area for each test image. In addition, the proposed method yielded the highest fDSC, the highest fJSC, and the highest AS for all tumor sizes, and the lowest HD for most tumor sizes.

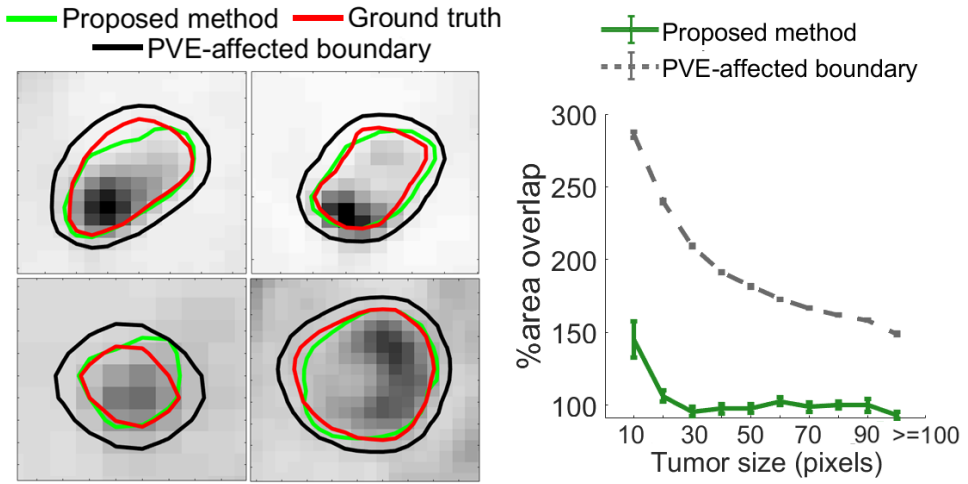


Fig. 8: Qualitative (left) and quantitative (right) comparisons between the PVE-affected boundaries and the tumor boundaries predicted by the proposed method.

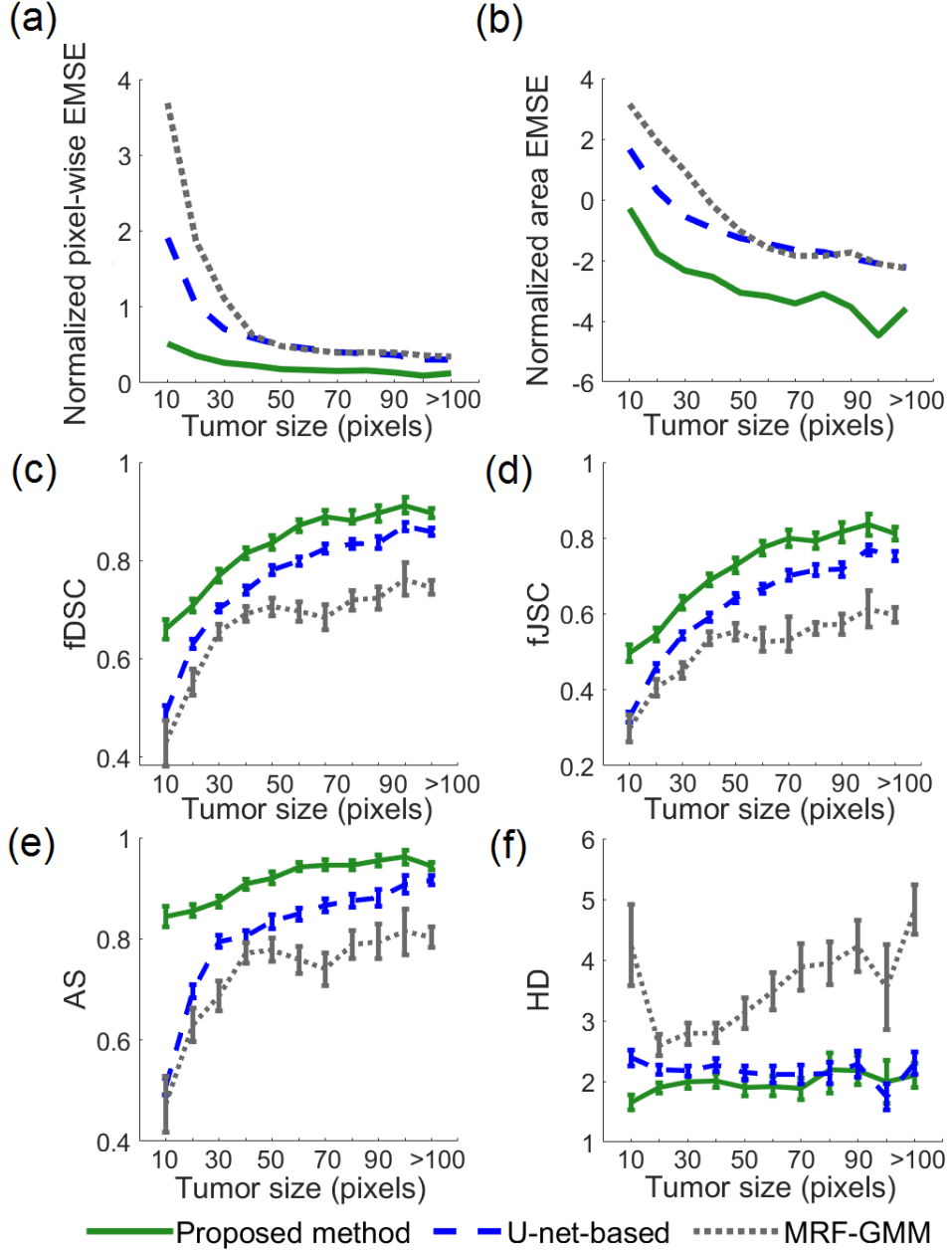


Fig. 9: Effects of varying the tumor size on the task of (a) estimating the tumor-fraction area, (b) estimating the entire tumor area (plot displayed in log scale for better visualization), and (c)-(f) evaluating the segmentation accuracy.

D. Evaluating the proposed method with clinical configurations

Fig. 10 shows the comparison of the segmentation accuracy between the proposed and the U-net-based method for the two scanners (Sec. III-C4). The proposed method significantly outperformed ($p < 0.01$) the U-net-based method for both scanners, on the basis of the fDSC,

fJSC, AS, and HD metrics. In addition, the segmentation accuracy was higher for the images obtained with the configuration of the Biograph Vision scanner, which has a higher resolution and lower voxel size than the Biograph 40.

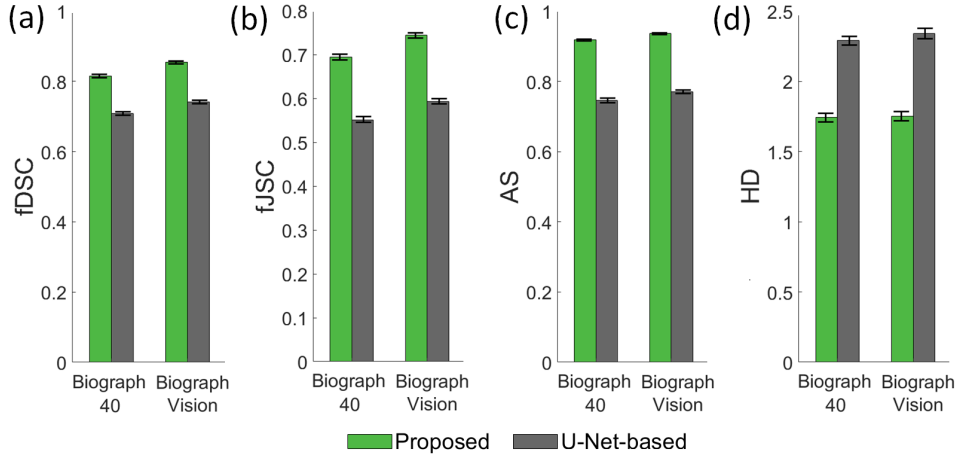


Fig. 10: Performance comparison of the proposed method and the U-net-based method with different clinical configurations using the (a) fuzzy Dice Similarity Coefficient, (b) fuzzy Jaccard Similarity Coefficient, (c) Area Similarity, and (d) Hausdorff Distance between the true and estimated segmentations.

V. DISCUSSIONS

In this manuscript, we proposed an estimation-based approach to segmentation. The objective of image segmentation is to partition an image into multiple regions of interest. Conventional segmentation methods perform this task by classifying each image pixel as belonging to a different region. These methods are apt to delineate images with very small pixel sizes, where each pixel can be assumed to contain only one region. However, in PET imaging, due to the larger pixel sizes and resultant TFEs, a pixel may contain more than one region. In an oncological PET image, a pixel may contain both the tumor and the background. The conventional classification-based approaches thus have an inherent limitation in segmenting these images. We address this limitation by framing the segmentation task as an estimation problem, where the fractional area that the tumor occupies in each pixel is estimated to yield the tumor boundary. Thus the proposed method still achieves the basic goal of image segmentation, although through a different approach.

Qualitatively, the proposed segmentation method demonstrated ability to accurately estimate the ground-truth tumor boundaries. In addition, the method yielded reliable segmentation even in

cases where tumors with complex intra-tumor heterogeneity. The method yielded non-pixelated continuous tumor contours due to the ability to estimate the continuous TFA values (Fig. 7). In contrast, the estimated contours yielded by conventional methods, including the U-net-based method, were pixelated and led to overestimation, especially for smaller tumors (Fig. 7). While a U-net-based method had previously demonstrated reliable segmentation by accounting for PVEs arising from system blur [12], the proposed method yielded a better match to the true tumor boundaries, thus demonstrating its ability to account for both sources of PVEs. More importantly, this superior performance emphasizes the importance of modeling the TFEs in PET segmentation.

The need to model TFEs was further demonstrated in the experimental results on evaluating the proposed method with different clinical configurations. For example, for the high-resolution Biogprah Vision scanner, the TFEs may be more dominant compared to system-resolution-related blur. We observed in Fig. 10 that the proposed method was more accurate compared to the U-net-based method for this scanner. This result also indicates that the proposed method yields more accurate segmentation when trained on images with higher resolution.

The performance of the proposed method was studied with realistic simulation studies. While these simulations generated highly realistic images as validated using observer studies, we still recognize that simulations may not be able to model all the tumor features and variabilities, and we thus term our study as a proof of concept. The results we obtained motivate evaluation of the method using physical-phantom and patient studies. In the physical-phantom studies, the ground-truth tumor boundaries can be obtained at high resolution from the CT images. Evaluation with patient data can be conducted by obtaining multiple manual segmentations from trained readers. These manual segmentations could then be combined using a technique such as the simultaneous truth and performance level estimation (STAPLE) technique [29], which yields a probabilistic estimate of the true segmentation. This estimate can then be used as ground truth for training and evaluation of the proposed method. The method can also be evaluated in patient studies by being trained on patient images obtained from a lower resolution PET scanner but with the ground-truth tumor definition obtained from a higher-resolution PET scanner. While this strategy may require the same patient to be imaged by both scanners, PET-insert-based technologies, such as virtual-pinhole PET [30], [31] can help address this issue by simultaneously acquiring both clinical and high-resolution images of the same tumor. Obtaining a large number of such patient images for training can be a challenge. To address this, the method could be pre-trained using realistic simulations or physical phantom studies, and then fine-tuned on actual patient

images. This strategy has demonstrated considerable success, even in segmenting PET images, as demonstrated in Leung et al. [12], which showed that even data from 25 patients was enough to achieve good segmentation accuracy.

The proposed segmentation method can benefit PET-based clinical applications that require tumor delineation such as PET-based radiotherapy planning [32]. Also, there is significant interest in evaluating PET-based volumetric markers of metabolic tumor volume (MTV) and total lesion glycolysis (TLG) as prognostic and predictive markers of therapy response [33]. Similarly, there is considerable interest in evaluating PET-based radiomic features as biomarkers [34], [35]. Measurement of these volumetric and radiomic features requires accurate tumor segmentation from PET images, as can be obtained using the proposed method. In fact, results in Fig. 6(c) on estimating the tumor area using the proposed method show that the method will accurately quantify the MTV and outperform conventional methods on that task.

As part of our evaluation study, we proposed a framework to generate simulated PET images containing tumors that were highly realistic, but had known ground-truth properties. The high realism of the simulated images motivates application of this simulation framework to a broader range of quantitative evaluation studies. These include quantitative evaluation of methods for image-segmentation [36] and metric quantification from images [37]. The images could also be used to evaluate methods for objective assessment of image quality for both detection [38] and quantification tasks [39]. Further, the proposed lumpy tumor model could be used to evaluate image-reconstruction methods. In all these studies, access to realistic tumor models will make the studies even more clinically relevant.

Our study has limitations. First, the method currently performs estimation-based segmentation on 2D PET image slices. While the method is applicable to 3D segmentation on a per-slice basis, this application would require manual input to select slices with tumors. In addition, while 2D segmentation is less computationally expensive and allows for availability of large amount of training data, 3D segmentation enables the method to learn spatial information about the whole tumor volume. Therefore, extending our proposed method to 3D segmentation is an important research direction. Second, the method currently considers cases where only a single tumor is present in the image. However, more generally, multiple tumors can be present. Thus, extending the method to segment multiple tumors simultaneously is another important research area. Further, the method does not incorporate tumor information from CT images when segmenting PET images. This incorporation would require generating realistic CT images

corresponding to the simulated PET images. However, incorporating information from CT images can provide a prior distribution of the TFAs for the estimation task. Thus, investigating the incorporation of CT images into the proposed method is another important research direction.

We propose our method in the context of segmenting oncological PET images. However, the methodology is general and can be extended to segment PET images for other applications, such as in cardiology and neurology. Further, the method can also be extended to segment images from other imaging modalities that have low resolution, such as single-photon emission computed tomography (SPECT) imaging and optical imaging modalities.

VI. CONCLUSION

In this manuscript, we proposed an estimation-based method to segment oncological PET images. The method yields posterior mean estimates of the tumor-fraction area for each pixel, which are then used to define continuous segmented tumor boundaries. Results demonstrated the ability of the method to reliably estimate the tumor-fraction areas and provide accurate tumor delineation on 2D PET images generated using a realistic and validated simulation framework. The method significantly outperformed commonly used PET segmentation methods, including a U-net-based method. Further, the method was relatively insensitive to partial-volume effects. The method demonstrated accurate performance with different clinical configurations. In conclusion, this proof-of-concept study demonstrates the efficacy of an estimation-based approach to PET segmentation.

ACKNOWLEDGMENTS

Financial support for this work was provided by the Department of Biomedical Engineering and the Mallinckrodt Institute of Radiology at Washington University in St. Louis and an NVIDIA GPU grant. We also thank the Washington University Center for High Performance Computing for providing computational resources for this project. The center is partially funded by NIH grants 1S10RR022984-01A1 and 1S10OD018091-01.

REFERENCES

- [1] A. K. Jha, E. Mena, B. S. Caffo, S. Ashrafinia, A. Rahmim, E. C. Frey, and R. M. Subramaniam, “Practical no-gold-standard evaluation framework for quantitative imaging methods: application to lesion segmentation in positron emission tomography,” *J. Med. Imaging*, vol. 4, no. 1, p. 011011, 2017.

- [2] G. J. Cook, G. Azad, K. Owczarczyk, M. Siddique, and V. Goh, "Challenges and promises of PET radiomics," *Int. J. Radiat. Oncol. Biol. Phys.*, vol. 102, no. 4, pp. 1083–1089, 2018.
- [3] E. Mena, S. Sheikbahaei, M. Taghipour, A. K. Jha, E. Vicente, J. Xiao, and R. M. Subramaniam, "18F-FDG PET/CT metabolic tumor volume and intra-tumoral heterogeneity in pancreatic adenocarcinomas: Impact of dual-time-point and segmentation methods," *Clin. Nucl. Med.*, vol. 42, no. 1, p. e16, 2017.
- [4] B. Foster, U. Bagci, A. Mansoor, Z. Xu, and D. J. Mollura, "A review on segmentation of positron emission tomography images," *Comput. Biol. Med.*, vol. 50, pp. 76–96, 2014.
- [5] P. Sridhar, G. Mercier, J. Tan, M. Truong, B. Daly, and R. Subramaniam, "FDG PET metabolic tumor volume segmentation and pathologic volume of primary human solid tumors," *Am. J. Roentgenol.*, vol. 202, pp. 1114–9, 05 2014.
- [6] M. Kass, A. Witkin, and D. Terzopoulos, "Snakes: Active contour models," *IEEE Proc, on Computer Vision and Pattern Recognition*, vol. 1, pp. 321–331, 01 1988.
- [7] T. Layer, M. Blaickner, B. Knäsl, D. Georg, J. Neuwirth, R. P. Baum, C. Schuchardt, S. Wiessalla, and G. Matz, "PET image segmentation using a Gaussian mixture model and Markov random fields," *EJNMMI physics*, vol. 2, no. 1, p. 9, 2015.
- [8] S. Belhassen and H. Zaidi, "A novel fuzzy C-means algorithm for unsupervised heterogeneous tumor quantification in PET," *Med. Phys.*, vol. 37, no. 3, pp. 1309–1324, 2010.
- [9] P. Blanc-Durand, A. Van Der Gucht, N. Schaefer, E. Itti, and J. O. Prior, "Automatic lesion detection and segmentation of 18F-FET PET in gliomas: a full 3D U-Net convolutional neural network study," *PLoS One*, vol. 13, no. 4, 2018.
- [10] X. Zhao, L. Li, W. Lu, and S. Tan, "Tumor co-segmentation in PET/CT using multi-modality fully convolutional neural network," *Phys. Med. Biol.*, vol. 64, no. 1, p. 015011, 2018.
- [11] M. Soret, S. L. Bacharach, and I. Buvat, "Partial-volume effect in PET tumor imaging," *J. Nucl. Med.*, vol. 48, no. 6, pp. 932–945, 2007.
- [12] K. Leung, W. Marashdeh, R. Wray, S. Ashrafinia, A. Rahmim, M. Pomper, and A. Jha, "A deep-learning-based fully automated segmentation approach to delineate tumors in FDG-PET images of patients with lung cancer," *J. Nucl. Med.*, vol. 59, no. supplement 1, pp. 323–323, 2018.
- [13] K. H. Leung, W. Marashdeh, R. Wray, S. Ashrafinia, M. G. Pomper, A. Rahmim, and A. K. Jha, "A physics-guided modular deep-learning based automated framework for tumor segmentation in PET images," 2020.
- [14] M. Hatt, C. C. Le Rest, A. Turzo, C. Roux, and D. Visvikis, "A fuzzy locally adaptive Bayesian segmentation approach for volume determination in PET," *IEEE Trans. Med. Imaging*, vol. 28, no. 6, pp. 881–893, 2009.
- [15] M. Hatt, F. Lamare, N. Boussion, A. Turzo, C. Collet, F. Salzenstein, C. Roux, P. Jarritt, K. Carson, C. Cheze-Le Rest *et al.*, "Fuzzy hidden Markov chains segmentation for volume determination and quantitation in PET," *Phys. Med. Biol.*, vol. 52, no. 12, p. 3467, 2007.
- [16] A. Creswell, K. Arulkumaran, and A. A. Bharath, "On denoising autoencoders trained to minimise binary cross-entropy," *arXiv preprint arXiv:1708.08487*, 2017.
- [17] H. H. Barrett and K. J. Myers, *Foundations of image science*. John Wiley & Sons, 2013.
- [18] G. Alain and Y. Bengio, "What regularized auto-encoders learn from the data-generating distribution," *J. Mach. Learn. Res.*, vol. 15, no. 1, pp. 3563–3593, 2014.
- [19] D. P. Kingma and J. Ba, "Adam: A method for stochastic optimization," *arXiv preprint arXiv:1412.6980*, 2014.
- [20] F. P. Kuhl and C. R. Giardina, "Elliptic Fourier features of a closed contour," *Comput. Gr. Image Process.*, vol. 18, no. 3, pp. 236–258, 1982.
- [21] N. Henscheid, E. Clarkson, K. J. Myers, and H. H. Barrett, "Physiological random processes in precision cancer therapy," *PLoS One*, vol. 13, no. 6, p. e0199823, 2018.

- [22] J. Rolland and H. H. Barrett, "Effect of random background inhomogeneity on observer detection performance," *J. Opt. Soc. Am. A*, vol. 9, no. 5, pp. 649–658, 1992.
- [23] C. Ma, B. Chen, L. Yu, C. W. Koo, S. Leng, E. A. Takahashi, J. G. Fletcher, D. L. Levin, R. S. Kuzo, L. D. Viers *et al.*, "Evaluation of a projection-domain lung nodule insertion technique in thoracic computed tomography," *J. Med. Imaging*, vol. 4, no. 1, p. 013510, 2017.
- [24] B. Chen, C. Ma, S. Leng, J. L. Fidler, S. P. Sheedy, C. H. McCollough, J. G. Fletcher, and L. Yu, "Validation of a projection-domain insertion of liver lesions into CT images," *Acad. Radiol.*, vol. 23, no. 10, pp. 1221–1229, 2016.
- [25] A. A. Taha and A. Hanbury, "Metrics for evaluating 3D medical image segmentation: analysis, selection, and tool," *BMC Med. Imaging*, vol. 15, no. 1, p. 29, 2015.
- [26] A. K. Jha, J. J. Rodriguez, R. M. Stephen, and A. T. Stoeck, "A clustering algorithm for liver lesion segmentation of diffusion-weighted MR images," in *2010 IEEE Southwest Symposium on Image Analysis Interpretation (SSIAI)*, May 2010, pp. 93–96.
- [27] S. Krinidis and V. Chatzis, "A robust fuzzy local information C-means clustering algorithm," *IEEE Trans. Image Process.*, vol. 19, no. 5, pp. 1328–1337, 2010.
- [28] E. De Bernardi, E. Faggiano, F. Zito, P. Gerundini, and G. Baselli, "Lesion quantification in oncological positron emission tomography: A maximum likelihood partial volume correction strategy," *Med. Phys.*, vol. 36, no. 7, pp. 3040–3049, 2009.
- [29] A.-S. Dewalle-Vignion, N. Betrouni, C. Baillet, and M. Vermandel, "Is STAPLE algorithm confident to assess segmentation methods in PET imaging?" *Phys. Med. Biol.*, vol. 60, no. 24, p. 9473, 2015.
- [30] A. J. Mathews, S. Komarov, H. Wu, J. A. O'Sullivan, and Y.-C. Tai, "Improving PET imaging for breast cancer using virtual pinhole PET half-ring insert," *Phys. Med. Biol.*, vol. 58, no. 18, p. 6407, 2013.
- [31] J. Jiang, K. Li, Q. Wang, K. Puterbaugh, J. W. Young, S. B. Siegel, J. A. O'Sullivan, and Y.-C. Tai, "A second-generation virtual-pinhole PET device for enhancing contrast recovery and improving lesion detectability of a whole-body PET/CT scanner," *Med. Phys.*, vol. 46, no. 9, pp. 4165–4176, 2019.
- [32] H. Zaidi, H. Vees, and M. Wissmeyer, "Molecular PET/CT imaging-guided radiation therapy treatment planning," *Acad. Radiol.*, vol. 16, no. 9, pp. 1108–1133, 2009.
- [33] N. Ohri, F. Duan, M. Machtay, J. J. Gorelick, B. S. Snyder, A. Alavi, B. A. Siegel, D. W. Johnson, J. D. Bradley, A. DeNittis *et al.*, "Pretreatment FDG-PET metrics in stage III non-small cell lung cancer: ACRIN 6668/RTOG 0235," *J. Natl. Cancer Inst.*, vol. 107, no. 4, 2015.
- [34] Y. Zhang, A. Oikonomou, A. Wong, M. A. Haider, and F. Khalvati, "Radiomics-based prognosis analysis for non-small cell lung cancer," *Sci. Rep.*, vol. 7, p. 46349, 2017.
- [35] E. Mena, M. Taghipour, S. Sheikbahaei, A. K. Jha, A. Rahmim, L. Solnes, and R. M. Subramaniam, "Value of intra-tumoral metabolic heterogeneity and quantitative 18F-FDG PET/CT parameters to predict prognosis, in patients with HPV-positive primary oropharyngeal squamous cell carcinoma," *Clin. Nucl. Med.*, vol. 42, no. 5, p. e227, 2017.
- [36] A. Le Maitre, W. P. Segars, S. Marache, A. Reilhac, M. Hatt, S. Tomei, C. Lartizien, and D. Visvikis, "Incorporating patient-specific variability in the simulation of realistic whole-body 18F-FDG distributions for oncology applications," *Proceedings of the IEEE*, vol. 97, no. 12, pp. 2026–2038, 2009.
- [37] V. Bettinardi, I. Castiglioni, E. De Bernardi, and M. Gilardi, "PET quantification: strategies for partial volume correction," *Clin. Transl. Imaging*, vol. 2, no. 3, pp. 199–218, 2014.
- [38] H. Gifford, "Efficient visual-search model observers for PET," *Br. J. Radiol.*, vol. 87, no. 1039, p. 20140017, 2014.
- [39] A. K. Jha, B. Caffo, and E. C. Frey, "A no-gold-standard technique for objective assessment of quantitative nuclear-medicine imaging methods," *Phys. Med. Biol.*, vol. 61, no. 7, p. 2780, 2016.